Journal of Electroanalytical Chemistry 750 (2015) 100–106

Contents lists available at ScienceDirect

Journal of Electroanalytical Chemistry

journal homepage: www.elsevier.com/locate/jelechem

# Determination of flow patterns in a rotating disk electrode configuration by MRI

Mariela Carpinella [a], Manuel I. Velasco [a], Emilia V. Silletta [a], Juan M. Ovejero [b], Sergio A. Dassie [b,*], Rodolfo H. Acosta [a,*]

[a] FaMAF-Universidad Nacional de Córdoba and IFEG-CONICET, 5000 Córdoba, Argentina
[b] Departamento de Fisicoquímica, Instituto de Investigaciones en Fisicoquímica de Córdoba (INFIQC), Facultad de Ciencias Químicas, Universidad Nacional de Córdoba, X5000HUA, Ciudad Universitaria, Córdoba, Argentina

ARTICLE INFO

*Article history:*
Received 28 January 2015
Received in revised form 14 May 2015
Accepted 16 May 2015
Available online 18 May 2015

*Keywords:*
MRI
Velocimetry
Taylor Couette cell
Rotating disk electrode

ABSTRACT

Velocity maps in an electrochemical cell model with a rotating disk electrode configuration were acquired by magnetic resonance imaging. This is one of the devices most widely used to characterize electrochemical reactions, where the relevant information needed is the velocity of the fluid ingoing the region of the electrode. Velocity maps of the whole cell were acquired with MRI for different rotating speeds and cell configuration. Results are in good agreement with previous data obtained by computational fluid dynamics (CFDs).



## 1. Introduction

Electrochemical cells with a rotating disk electrode (RDE) configuration are widely used to characterize electrochemical reactions [1–6]. Particularly, in studying electrode reaction kinetics and mechanisms has shown their advantages in measuring stoichiometric number of electron transfer in the electrochemical reaction, bulk concentration and diffusion coefficient, reaction kinetic constant and reaction intermediates. RDE is amenable to rigorous theoretical treatment and is easy to construct with a variety of electrode materials. In this setup, mass transfer and the associated velocity profiles in the vicinity of the electrode play a main role in the analysis of the information obtained. The spinning disk drags the fluid at its surface along with it and, because of centrifugal force, flings the solution outward from the center in a radial direction. The fluid at the disk surface is replenished by a flow normal to the surface. This fluid flow has been described several decades ago by Levich [7] based on the approximate analytical solution introduced by von Karman [8] and Cochran [9], who used a simplified model under the assumption of an infinite cell and an electrode of endless dimensions and negligible thickness. As the experimental cell parameters are neglected in these models, it is valid to ask how accurate is the use of this equation in real systems, where liquids are confined and flows are highly dependent on the experimental setup.

This question has been mainly addressed using computational fluid dynamic (CFD) models. Two main CFD models can be used, two-dimensional models which are characterized with axisymmetric representation [10,11] and three-dimensional models [12–14] where a representation of the whole cell is performed [15]. In these works, authors compare their results with the fluid flow pattern calculated with analytical expressions obtained by Cochran [10,11] and focus their attention in establish which factors cause the asymmetry in flow patterns [12,13]. Recently, Alexiadis et al. [14]showed that even though the Cochran equation does not describe correctly the velocity profiles over the whole cell, it provides an accurate representation of the flow near the electrode, thus the Levich equation can still be employed for electrochemical analysis, where the concentrations gradients due to electrochemical reactions are typically contained. Gonzalez et al. [12] addressed the problem of flow determination near the rotating rod containing the electrode for different configurations using 3D CFD and experimental optical methods. Asymmetric flow patterns were shown and a way to correct the Levich equation was proposed.

There is an outstanding lack of experimental data on flow patterns inside electrochemical cells with RDE configuration. This is mainly because an experimental determination of the flow is difficult due to cell geometry, electrode dimensions, and the

* Corresponding authors.
*E-mail addresses:* sdassie@fcq.unc.edu.ar (S.A. Dassie), racosta@famaf.unc.edu.ar (R.H. Acosta).

http://dx.doi.org/10.1016/j.jelechem.2015.05.018
1572-6657/

requirement of optically transparent flows. Only recently, 1D velocity determinations were carried out using Laser Doppler Anemometry [10] and optical determinations of the flow effects near the rotating rod were compared to numerical simulations [12]. Magnetic resonance imaging (MRI) is a suitable tool for this purpose as it is non-invasive and non-destructive. In particular the use of tracer particles is not needed as spin bearing nuclei, in general $^1$H, which is part of the flowing liquid, can be used to determine the flow patterns. This has two benefits, on one hand the flow is not disturbed by impurities, and on the other hand any liquid, even non-transparent liquids can be used. Imaging results can also be combined with spectroscopic information provided by NMR, providing spatially resolved chemical information. Recently, Ilott et al. [16] presented the first *in situ* experiments showing localized information of the electrolyte ions in real time for a working capacitor of standard geometry. It has also been shown that MRI is able to map concentration gradients and visualize electrochemical processes in electrochemical cells containing bulk metals [17].

MRI has been extensively used for the characterization of the flows in a wide variety of systems [18–20]. In particular, Couette cells (CC) present similar aspects as that of a RDE. A CC is a device composed of two concentric rotating cylinders, where a large variety of flows can occur upon variations of the fluid properties, system geometry, or rotation rates. For slow rotational speeds the flow pattern is a 1D laminar azimuthal flow without velocity components in the axial or radial directions. For rotation speed above a critical value a hydrodynamic instability occurs and counter-rotating vortices appear superimposed on the azimuthal rotation of the liquid, known as Taylor vortices. The device is denominated Taylor–Couette cell (TCC), and the corresponding flow is known as a Taylor vortex flow (TVF) [21,22]. Several works using MRI were carried out on CCs, for instance TVF and even translating vortex flows have been measured by synchronizing the imaging sequence with the rotations [23] or axially stratified two-fluid systems velocities were determined [24].

In this work we present for the first time flow measurements in an electrochemical cell model with a RDE configuration by MRI. We use a TCC with a TVF to show the performance of our imaging system, as the flow pattern of this system is known a priori, this is used for velocity calibration in the three orthogonal axes. The cell can be modified by changing the length of the rotating rod in order to generate a RDE configuration. Velocity maps in three orthogonal directions are presented and velocities ingoing on the electrode are discussed for different Reynolds numbers.

## 2. Materials and methods

### 2.1. Magnetic resonance imaging

The aim of this section is to provide a simplified overview of the basic elements involved in the process of using nuclear magnetic resonance for imaging. For detailed descriptions of the method, see Refs. [25,26] and specific applications in electrochemistry in Ref. [27]. NMR is based on the fact that nuclear spins undergo a precession around the direction of the magnetic field induced by the magnet ($B_0$). MRI relies on the use of an extra set of magnetic fields, which are designed to change linearly with space. In general three independent gradients are used, each of which encodes an orthogonal direction. These magnetic field gradients ($\boldsymbol{G}$) give rise to a frequency that depends on the position ($\boldsymbol{r}$) as:

$$\omega_0(\boldsymbol{r}) = \gamma(B_0 + \boldsymbol{r}\cdot\boldsymbol{G}), \tag{1}$$

where $\gamma$ is the nuclear gyromagnetic ratio of the observed isotope (e.g. $^1$H, $^{19}$F, $^7$Li). If signal decay is recorded under the action of one of such gradients, a Fast Fourier Transform (FFT) will render a projection of the object in one direction, this is usually referred to as a 1D image. In order to obtain a 3D image of an object two alternative methods can be applied. A set of 2D images, in which different slices of the object are acquired can be used, or a full 3D set of data can be obtained. The former method is in general applied to study a specific region of interest and is chosen in favor of a 3D image as this latter is in general very time consuming.

The MRI sequence used in this work is a 2D spin echo sequence with spin warp sampling (see Fig. 1). A spin-echo is generated by a shaped refocusing 180° pulse applied at a time $t_E/2$ after the excitation pulse, and in the presence of a magnetic field gradient ($G_{\text{slice}}$). The magnetization from a determined region in space is acquired, in this case a Gaussian shaped pulse will refocus the magnetization only from spins located in a Gaussian region of space [26]. Acquisition of $N$-data points is carried out in the presence of a magnetic field gradient ($G_{\text{read}}$), so that an accumulation of phase in one dimension of the $\boldsymbol{k}$-space is achieved (read direction). On the second direction experiments are carried out changing the values of a field gradient orthogonal to $G_{\text{read}}$ ($G_{\text{phase}}$) as shown in the fourth line of Fig. 1. In this way an $N \times M$ data set, representing the $\boldsymbol{k}$-space, is acquired. A 2D FFT algorithm will return a representation of 2D spin density over the selected slice. The direction of read, phase and slice gradients can be chosen arbitrarily.

### 2.2. Velocity maps

If the spin bearing molecules are moving during the application of a magnetic field gradient, an extra accumulation in the phases will be produced [28]. In this work a pair of bipolar gradients were applied after the 180° refocusing pulse (see last line in Fig. 1). The application of a pair of gradients imparts a phase proportional to the displacement of the sample in the direction in which the gradients are applied. This phase depends on the gradient intensity ($G_{\text{vel}}$), the pulse time duration ($\delta$) and the spacing between them ($\Delta$). For instance, the phase introduced by a gradient applied in the $z$ direction can be written as:

$$\phi = \int_0^{\delta} \gamma G_{\text{vel}}(t) z(t) dt. \tag{2}$$

For the bipolar pulses sketched in Fig. 1, this equation reduces to:

$$\phi = \gamma G_{\text{vel}} \left[ \int_0^{\delta} z(t)dt - \int_{\Delta}^{\delta+\Delta} z(t)dt \right]. \tag{3}$$

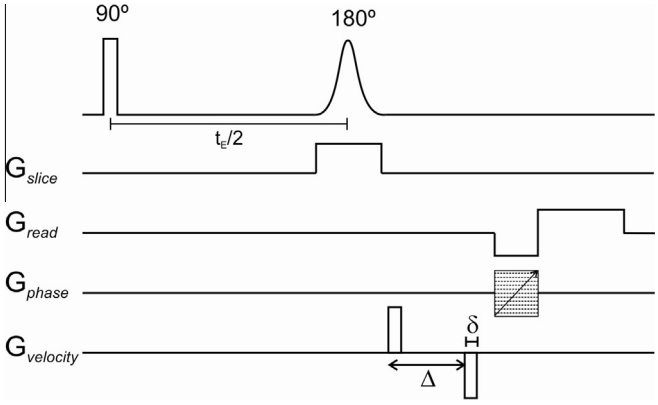


**Fig. 1.** Spin echo sequence used to obtain the velocity maps. Acquisition is performed on the center of a spin echo, formed at a time $t_E$. In this work the slice direction was taken along $y$, read gradients along $z$ and phase gradients along $x$. The velocity gradients are switched to different directions according to the experiment.

Evidently, if the nuclei are static the total accumulated phase is zero, however, if nuclei are moving with a stationary velocity, $\boldsymbol{v}$, the net phase can be written, in a general case as [29,30]:

$$\phi = \gamma\delta\Delta G_{vel} \cdot \boldsymbol{v} \quad (4)$$

It must be noted that even though this gradient is plotted in a different line in Fig. 1, it will be applied in one of the imaging directions. Velocity maps in a given spatial direction are obtained by calculating the phase difference between a reference image measured without velocity gradients and a second image measured with the bipolar gradient pair applied along the desired spatial direction [25]. The phase of the signal of both images is subtracted and the pixel by pixel phase difference is converted to velocities using Eq. (4), where the velocity of the nuclei contained in a volume element, or voxel, is considered to be stationary.

### 2.3. Experimental consideration on velocity MRI

There is a variety of factors that can influence the performance of MRI in the determination of velocities inside an electrochemical cell. Electrochemical experiments usually involve aqueous ionic systems in low concentrations, which can either be organic or inorganic, paramagnetic or non-paramagnetic. The main effect of the presence of ions on NMR is a change on the relaxation times, which depends on the ion concentration and on the paramagnetic characteristics. As electrochemistry is very sensitive, these concentrations are in general low, inducing minor changes in the relaxation times. However, in the presence of paramagnetic ions, these changes can be significant.

The spin–lattice relaxation time ($T_1$) is the system characteristic time in which equilibrium with the magnetic field is established. In MRI, this time accounts for the interval in which an excitation can be repeated, setting the overall image acquisition time. For pure water at room temperature and 7 Tesla $T_1 \sim 3$ s, while depending on the ion type and concentration $T_1$ can be in the order of hundreds of milliseconds. This effect turns out to be extremely beneficial as the images can be acquired in a shorter time.

Codification of velocities relies on the use of the accumulated phase described in Eq. (4). The intensity and duration of the gradients are set as to impart maximum phases ranging from $-\pi$ to $\pi$, where the sign determines the direction of the flow related to the direction of the velocity gradient [25]. This sets a maximum possible speed encoding, or field of flow (FOF). The values of $\delta$, $\Delta$ and $G_{vel}$ must be set in order to render an optimum velocity encoding, where the two limiting parameters are $\Delta$ and $G_{vel}$. For low velocity encoding large values for $\Delta$ and $G_{vel}$ are generally required. Typical gradients available in MRI systems range between 1 and 3 T/m and are set by the hardware, i.e., the gradient coils and current amplifiers. Upon setting a maximum gradient value, a minimum value of $\Delta$ is determined to achieve a correct codification. This duration cannot exceed a maximum value which is set by the sequence timing ($t_E$), and is mainly influenced by the transversal or spin–spin relaxation time ($T_2$). This is the characteristic time in which a signal decays during detection. The relationship between $T_2$ and the ion concentration is similar to that of $T_1$. For velocities in the order of 10 mm/s $T_2$ values over 50 ms are in general sufficient. For high velocities determination the main constraint is not given by the equipment, but from the image resolution. It is generally accepted that a molecule must not travel more than half a pixel size during data acquisition, which is the time in which $G_{read}$ is on, in order to achieve a correct velocity codification. For instance, for a resolution of 150 μm and a typical acquisition time of 600 μs a maximum velocity of 125 mm/s can be correctly encoded.

Another issue associated to electrochemical studies in MRI, is the presence of electrodes. Metallic components within the sample may generate image artifacts due to changes in the rf field, magnetic susceptibility and the presence of eddy currents [17,27]. As two images are necessary to obtain the velocity map these artifacts will in principle cancel out as they are equal in both, providing that the induced distortion is not strong enough to locally cancel the signal.

### 2.4. Experimental Setup

All experiments were carried out at 7.05 Tesla ($\nu_0$ = 300.13 MHz) in an Oxford superconducting magnet operated with a Kea2 (Magritek GmbH) console. A 3D gradient coil system (Bruker GmbH) with maximum gradients of 1.5 T/m was used. Radiofrequency excitation and detection was carried out with a 25 mm inner diameter Bruker GmbH birdcage coil with a length of 37 mm. A hard 90° pulse of 250 μs and a 180° Gaussian selective pulse of 600 μs of duration were used.

The system schematized in Fig. 2 was built from polyacetal resin and used in all the experiments. The exterior cylinder, with internal radius $R_2$ = 7.85 mm is static, while the inner cylinder, with radius $R_1$ = 3 mm, can rotate and its length can be modified in order to achieve a TCC or RDE configuration. The total height of the cell was $H_1 + H_2$ = 77 mm. The container was filled with a sample of deionized water doped with $CuSO_4$ to reduce $T_1$ to approximately 130 ms, resulting in a $T_2$ = 100 ms. The magnetic field homogeneity was such that the NMR signal decays with a characteristic time of 10 ms. For the TCC measurements $H_1 = 0$ and for the RDE configuration the position of the inner rod was changed such that $H_1$ = 15 mm. Two different rotation speeds were used: 31.4 and 94.2 Hz.

The field of view was set to (40 × 20) mm in the $z$ and $x$ directions. A 2 mm slice in $y$ direction was excited and detected. Matrices of 256 × 128 points were acquired, giving rise to a resolution of (0.156 × 0.156 × 2) mm$^3$. Four images were acquired for

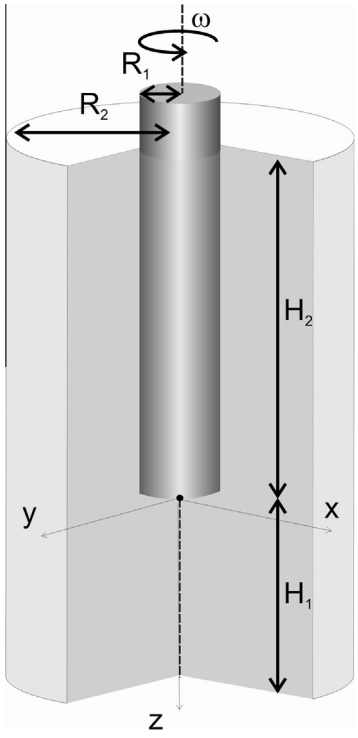


**Fig. 2.** Schematic representation of the cell used in the experiments. The position of the rotating rod can be changed to achieve a Couette cell ($H_1 = 0$) or a rotating disk electrode ($H_1$ = 15 mm) configuration.

each configuration and rotating speed, one reference without velocity gradient and three images with velocity gradients in each direction. The most relevant parameters of the pulse sequence were the following: echo time: $t_E = 13$ ms, $\delta = 1$ ms and $\Delta = 2.3$ ms for encoding velocities over 40 mm/s, otherwise $t_E$ was set to 15 ms and $\Delta = 3.1$ ms. In all the cases, the dwell time was 5 μs and the acquisition time was 1.28 ms. The total experimental time for a complete 3D velocity map was of 34 min, in which 8 acquisitions were acquired and averaged. A waiting period of ten minutes was introduced between the startup of the rotations until the acquisition of the images. All experiments were repeated at least three times and showed to be reproducible with dispersion in the velocity values of 5%.

## 3. Results and discussion

### 3.1. TCC configuration

Initially we describe the results in the TCC with a fixed outer cylinder and the inner cylinder rotating at 31.4 Hz. This system has cylindrical symmetry where radial velocities correspond to $v_x$ and azimuthal velocities correspond to $v_y$. The individual components ($x$ and $z$) of the rotating vortices are observed in Fig. 3a and b respectively, where a 2 mm slice in the $y$ direction is excited. Radial velocities show a periodic behavior alternating its orientation towards and from the rotating cylinder, with maximum velocities up to 27 mm/s in the jets moving away from the rotating rod. The flow in $z$ presents velocities going up and down on each side of the rotating cylinder, where maximum velocities of 20 mm/s occur near the rotating rod. Combining these data sets render a vector plot map where the rotating vortices are clearly observed (see Fig. 3c). A maximum velocity in the azimuthal direction of 93 mm/s is determined (Fig 3d), in agreement with the velocity for the liquid in contact with the inner cylinder speed of 94 mm/s. The velocity intensity decreases with increasing distance from the center of the system until it practically cancels out on the surface of the outer cylinder. The pattern for out of plane and in-plane velocities is the same with opposite directions. The undulations in the velocity distributions are in accordance with the presence of Taylor vortices. The $z$ velocity profile can be used in the determination of the vortices sizes. Fig. 4 shows the velocities extracted from a line of the $z$ profile at 31.4 Hz. The vortices are symmetrical and the size is even throughout the sample with an average value of 6 mm. In this way MRI can be used to obtain information of the flow that takes place in the system under study in a qualitative way: vortex shape or flow symmetry for instance, and in a quantitative way: velocity values or vortex size.

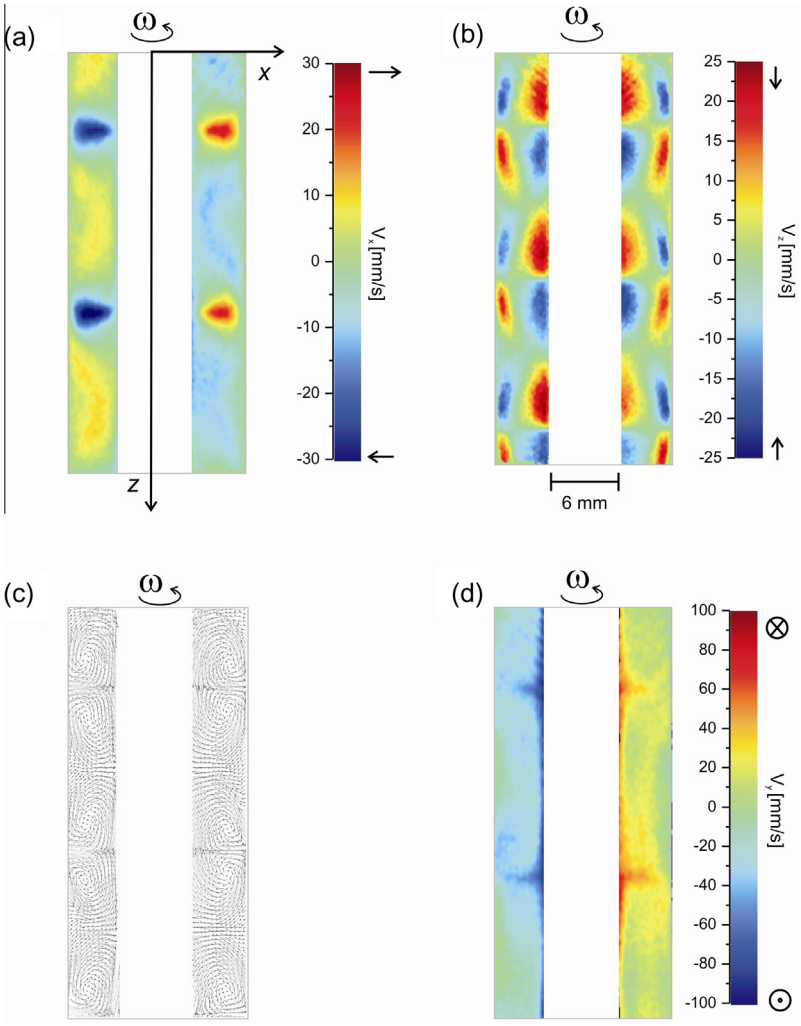


**Fig. 3.** Velocity maps of a water/glycerol system in a Couette cell for a rotation rate of 157 Hz, $H_1 = 0$, $H_2 = 77$ mm and Re = 44 (a) velocity along $x$ direction and (b) $z$ direction. (c) Vector plot constructed with $v_x$ and $v_z$. (d) Velocities in the azimuthal direction ($v_y$).

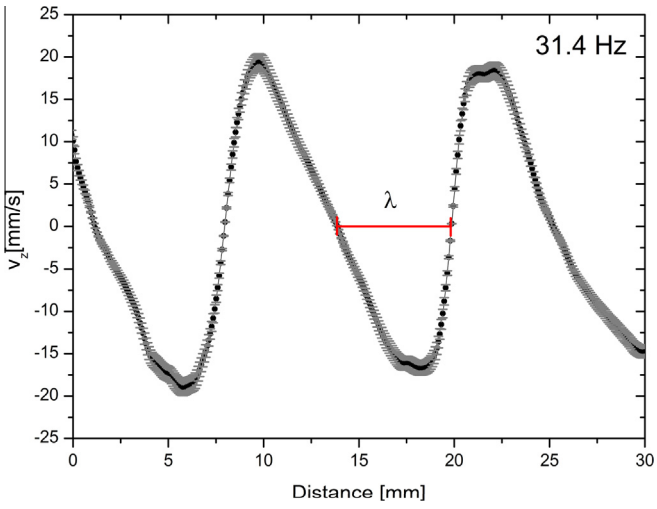


**Fig. 4.** Velocity profile along the $z$ direction for a TCC rotating at 31.4 Hz. The vortex size $\lambda$ can be directly determined from the plot as the distance between two points with $v_z = 0$.

### 3.2. RDE configuration

We now turn our attention to the flow pattern generated inside a RDE cell. Fig. 5 shows the velocity maps corresponding to velocities in a 2 mm $xz$ plane for two different velocity values and $H_1 = 15$ mm. A circulation of fluid under the rotating electrode can be clearly observed; the liquid goes towards the bottom of the cell ($z$-velocities in Fig. 5c) through the outer region and returns to the electrode through the center of the cell. This flow represents the main mass transfer process that takes place in the system. The most striking feature is that for the low rotation speed a great asymmetry in the flow is observed, while as the rotation speed increases a more symmetrical pattern is obtained.

Fig. 5 also shows how the fluid behaves in the recirculation area surrounding the rotating electrode [14]. In order to obtain a good representation of the lower velocities in the cell, the FOF was set to 45 mm/s. For this reason the higher velocities near the rotating rod are appear saturated in the color scale. Nevertheless it is clear that near the lateral walls of the rotating rod the flow direction is going upward, which is in disagreement with early predictions done by Blurton and Riddiford [31] and confirms the flow patterns predicted by Gonzalez et al. [12] and Dong et al. [11]. This is also in agreement with the velocity field in the 3D cell obtained from CFD (see Supplementary material).

A quantitative representation of the resulting flow in the axis below the center of the rotating rod is better understood through the use of dimensionless variables [32]. In order to describe the velocity field, $u(r, \phi, z)$, in cylindrical coordinates, six dimensional variables are needed: $(H_1, H_2, R_1, R_2, \nu, \omega)$, where $\nu$ and $\omega$ are the fluid viscosity and rotation speed respectively. The system coordinates and velocity components can be expressed in a dimensionless way as $(\rho, \phi, \zeta)$ and $(\gamma, \vartheta, \psi)$ respectively. For the description of axial velocities the Reynolds number ($\mathrm{Re} = \omega R_1^2/\nu$), axial coordinate ($\zeta = z\sqrt{\omega/\nu}$) and velocity ($\psi = \mathrm{v}_z/\sqrt{\omega\nu}$) are used. Two different Reynolds numbers were obtained by changing the rotation speed. Data from pixels of the central line of the RDE were extracted and are plotted in Fig. 6. The experimental velocities are higher than those predicted by the Cochran equation for the lower Reynolds number ($\mathrm{Re} = 280$), as calculated by Alexiadis et al. [14]. The Cochran equation predicted a plateau at $\psi = 0.88$ while the experimental value shows a maximum at $\psi = 2$, in agreement with the maximum value reported by Alexiadis et al. [14]. As

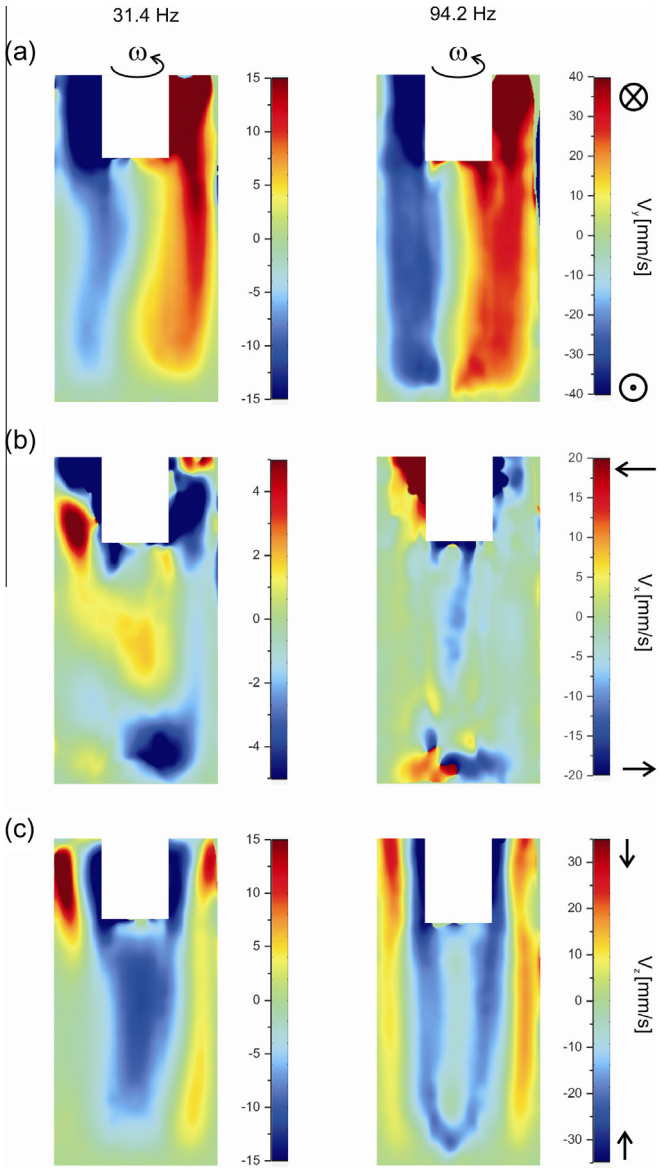


**Fig. 5.** Velocity maps in a RDE cell ($H_1 = 15$ mm) for a rotation speed of 31.4 Hz and 94.2 Hz. (a) Velocity along $x$ direction, (b) $y$ direction and (c) $z$ direction. As the rotation speed increases a more symmetric flow pattern is observed.

the Reynolds number increases the presence of asymmetries is depicted by an increase in the velocities at the bottom of the cell, where the non-slip condition on the surface is satisfied. For $\mathrm{Re} = 850$ velocity follows the Cochran equation up to $\zeta = 120$. The increase in velocities near the bottom of the cell may arise from asymmetries in the flow. This behavior showed to be reproducible in several repetitions and even when the rotational speed direction is inverted. Gonzalez et al. have recently predicted [12] a similar patterns and are indicated in the work of Mandin et al. [10] who measured oscillations in the velocity amplitudes in the bottom of the cells.

The Cochran equation that describes the velocity profile in RDE systems has been used to determine the charge transfer rate constant from experimental data. In the particular case of fast reaction rates, the Levich equation can be applied to calculate the limiting current [33–35]. On this regard, it is important to remark that electrochemical signals are mainly determined by the velocity field in the vicinity of the electrode, since the electrochemical reactions are

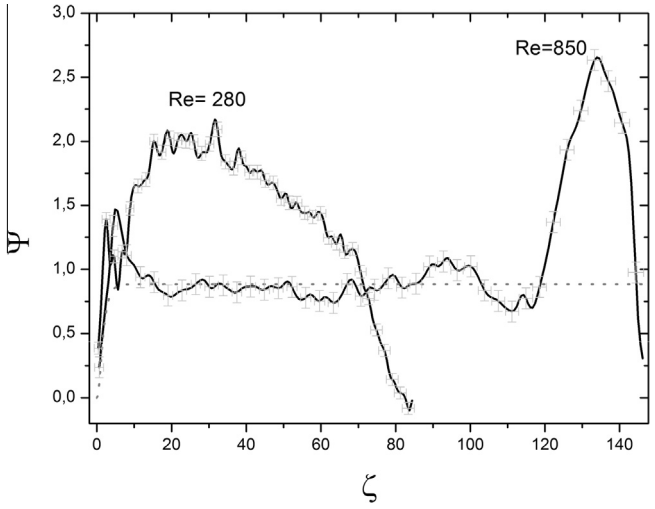


**Fig. 6.** Dimensionless velocity along the central axis at two values of Reynolds number. The error bars are calculated propagating the uncertainties in the velocity determination and the rotational speed. For the low Reynolds number (31.4 Hz) a behavior predicted by Alexiadis et al. [14] is observed. For larger Reynolds numbers larger velocities are present in the bottom of the cell and a significant region in the center of the cell satisfies the constant behavior of the Cochran equation (dashed).

mostly located in this region. For this reason, the Levich equation is a reasonable practical approximation for calculating the limiting current in a RDE system because near the electrode the flow is not necessarily affected by the recirculation regions. As a proof of concept, Fig. 7 shows the experimental velocity profiles at two Reynolds numbers in the vicinity of the rod-like electrode compared to the profile calculated according to the Cochran equation. Clearly, the velocity profiles determining the arrival of electro-active species at the electrode are comparable to that predicted by the Cochran equation for both Reynolds numbers. Therefore, Levich equation can be used to predict the electrochemical signals (i.e., the limiting current) measured with very fast reaction rates at the RDE with the same electrochemical configuration as in the studied system. In fact, we are currently dedicated to analyze different experimental methodologies to determine more accurately the velocity fields in the vicinity of the rod-like electrode.

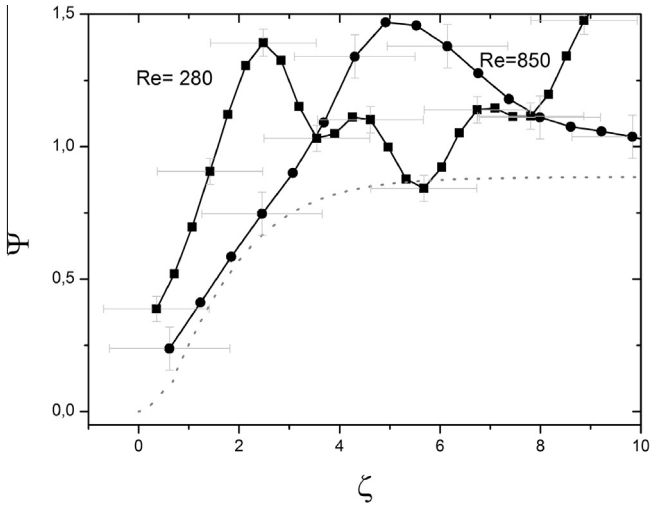


**Fig. 7.** Dimensionless velocity along the central axis at two values of Reynolds number in the vicinity of the rotating electrode. Squares correspond to Re = 280 and circles to Re = 850. The dashed line corresponds to the Cochran equation.

## 4. Conclusions

Velocities in RDE electrochemical cells can be accurately determined by MRI, and the presented results are in good agreement with previous ones obtained by CFD methods. In this work we used one of the most robust, yet time consuming pulse sequences normally used for this purpose. However, fast velocity determination schemes can readily be implemented where a complete velocity map could be acquired in the order of hundreds of milliseconds. We envision the MRI will become a powerful tool in the determination of fluid properties in RDE configuration were the performance of different cell designs can be directly determined and thus improve the mass transfer to the electrode.

## Acknowledgments

We thank the financial support from CONICET, SeCyT Universidad Nacional de Córdoba, ANPCYT PICT 2010-1096/2274 and PICT 2012-1820. M. Carpinella, M.I. Velasco, E.V. Silletta and J.M. Ovejero thank CONICET for their fellowships.

## Appendix A. Supplementary data

Supplementary data associated with this article can be found, in the online version, at http://dx.doi.org/10.1016/j.jelechem.2015.05.018.

## References

[1] K.F. Blurton, A.C. Riddiford, Shapes of practical rotating disc electrodes, J. Electroanal. Chem. (1959) 10 (5–6) (1965) 457–464.
[2] F. Opekar, P. Beran, Rotating disk electrodes, J. Electroanal. Chem. Interfacial Electrochem. 69 (1) (1976) 1–105.
[3] A.J. Bard, L.R. Faulkner, 2nd ed., Electrochemical Methods: Fundamentals and Applications, J.W.S. Inc, New York, 2001.
[4] C.M.A. Bret, A.M.O. Bret, 2nd ed., Electrochemistry: Principles, Methods, and Applications, O.U. Press, Oxford, 1994.
[5] C.M.A. Bret, A.M.O. Bret, 2nd ed., in: C.H.B.a.R.G. Compton (Ed.), Comprehensive Chemical Kinetics, Elsevier, Amsterdam, 1986.
[6] J. Newman, K.E. Thomas-Alyea, 3rd ed., Electrochemical Systems, John Willey & Sons Inc., New York, 2004.
[7] B. Levich, The theory of concentration polarization, Acta Physicochim. Urss 17 (1942) 257–307.
[8] T.H.v. Karman, Über laminare un turbulente Reibung, Zeitschrift für Angewandte Mathematik un Mechanik 1 (1921) 233–252.
[9] W.G. Cochran, The flow due to a rotating disc, Math. Proc. Cambridge Philos. Soc. 30 (3) (1934) 365–375.
[10] P. Mandin, T. Pauporté, P. Fanouillère, D. Lincot, Modelling and numerical simulation of hydrodynamical processes in a confined rotating electrode configuration, J. Electroanal. Chem. 565 (2) (2004) 159–173.
[11] Q. Dong, S. Santhanagopalan, R.E. White, A comparison of numerical solutions for the fluid motion generated by a rotating disk electrode, J. Electrochem. Soc. 155 (9) (2008) B963–B968.
[12] J. Gonzalez, C. Real, L. Hoyos, R. Miranda, F. Cervantes, Characterization of the hydrodynamics inside a practical cell with a rotating disk electrode, J. Electroanal. Chem. 651 (2) (2011) 150–159.
[13] C.A. Real-Ramirez, R. Miranda-Tello, L.F. Hoyos-Reyes, J.I. Gonzalez-Trejo, Hydrodynamic characterization of an electrochemical cell with rotating disc electrode: a three-dimensional biphasic model, Int. J. Chem. Reactor Eng. 8 (2010).
[14] A. Alexiadis, A. Cornell, M.P. Dudukovic, Comparison between CFD calculations of the flow in a rotating disk cell and the Cochran/Levich equations, J. Electroanal. Chem. 669 (2012) 55–66.
[15] C.A. Real-Ramirez, J.I. Gonzalez-Trejo, in: J. Zhu (Ed.), Hydrodynamic Analysis of Electrochemical Cells, Computational Simulations and Applications, 2011, ISBN: 978-953-307-430-6.
[16] A.J. Ilott, N.M. Trease, C.P. Grey, A. Jerschow, Multinuclear in situ magnetic resonance imaging of electrochemical double-layer capacitors, Nat. Commun. 5 (2014) 4536.
[17] M.M. Britton, Magnetic resonance imaging of electrochemical cells containing bulk metal, Chem. Phys. Chem. 15 (9) (2014) 1731–1736.
[18] E.L. Hahn, Detection of sea-water motion by nuclear precession, J. Geophys. Res. 65 (2) (1960) 776–777.
[19] N.J. Pelc, M.A. Bernstein, A. Shimakawa, G.H. Glover, Encoding strategies for 3-direction phase-contrast MR imaging of flow, J. Magn. Reson. Imaging 1 (4) (1991) 405–413.

[20] L.F. Gladden, A.J. Sederman, Recent advances in Flow MRI, J. Magn. Reson. 229 (2013) 2–11.
[21] G.I. Taylor, Stability of a viscous liquid contained between two rotating cylinders, Philos. Trans. R. Soc. London, A 223 (605) (1923) 289–343.
[22] C.D. Andereck, S.S. Liu, H.L. Swinney, Flow regimes in a circular Couette system with independently rotating cylinders, J. Fluid Mech. 164 (1986) 155–183.
[23] A. Vallatos, M.C.T. Wilson, A.F. Taylor, M.M. Britton, Characterising stationary and translating vortex flow using magnetic resonance, EPL (Europhys. Lett.) 99 (6) (2012) 68001.
[24] A. Broadbent, J. Mullin, S. Codd, J. Dockery, J. Seymour, Pulsed gradient spin echo nuclear magnetic resonance measurement and simulation of two-fluid Taylor vortex flow in a vertically oriented Taylor–Couette device, Appl. Magn. Reson. 42 (1) (2012) 137–152.
[25] P.T. Callaghan, Translational dynamics and magnetic resonance: principles of pulsed gradient spin echo NMR, Oxford University Press, Oxford, New York, 2011.
[26] E.M. Haacke, R.W. Brown, M.R. Thompson, R. Venkatesan, Magnetic Resonance Imaging: Physical Principles and Sequence Design, John Wiley & Sons Inc, New York, 1999.
[27] W.K. Feindel, Magnetic resonance imaging (MRI) techniques for polymer electrolyte membrane and direct alcohol fuel cell characterization, in: C. Hartnig, C. Roth (Eds.), Polymer electrolyte membrane and direct methanol fuel cell technology, Woodhead Publishing Ltd., Philadelphia, 2012.
[28] K. Kose, One-shot velocity mapping using multiple spin-echo EPI and its application to turbulent flow, J. Magnetic Reson. (1969) 92 (3) (1991) 631–635.
[29] P.R. Moran, A flow velocity zeugmatographic interlace for NMR imaging in humans, Magn. Reson. Imaging 1 (4) (1982) 197–203.
[30] M. O'Donnell, NMR blood flow imaging using multiecho, phase contrast sequences, Med. Phys. 12 (1) (1985) 59–64.
[31] K.F. Blurton, A.C. Riddiford, Shapes of practical rotating disc electrodes, J. Electroanal. Chem. 10 (5–6) (1965) 457–464.
[32] V.G. Levich, Physicochemical Hydrodynamics, Prentice-Hall, Englewood Cliffs, N.J., 1962.
[33] C.M.A. Brett, A.M.O. Brett, Electrochemistry: Principles, Methods, and Applications, Oxford University Press, 1993, p. 456.
[34] A.J. Bard, L.R. Faulkner, 2nd ed., Electrochemical Methods Fundamentals and Applications, Wiley, 2001.
[35] J. Newman, K.E. Thomas-Alyea, 3rd ed., Electrochemical Systems, Wiley, 2004.